

Gradient Networks for Universal Magnetic Modeling of Synchronous Machines

Junyi Li, Tim Foßner, Floran Martin, Antti Piippo, and Marko Hinkkanen, *Fellow, IEEE*

Abstract—This paper presents a physics-informed neural network approach for dynamic modeling of saturable synchronous machines, including cases with spatial harmonics. We introduce an architecture that incorporates gradient networks directly into the fundamental machine equations, enabling accurate modeling of the nonlinear and coupled electromagnetic constitutive relationship. By learning the gradient of the magnetic field energy, the model inherently satisfies energy balance (reciprocity conditions). The proposed architecture can universally approximate any physically feasible magnetic behavior and offers several advantages over lookup tables and standard machine learning models: it requires less training data, ensures monotonicity and reliable extrapolation, and produces smooth outputs. These properties further enable robust model inversion and optimal trajectory generation, often needed in control applications. We validate the proposed approach using measured and finite-element method (FEM) datasets from a 5.6-kW permanent-magnet (PM) synchronous reluctance machine. Results demonstrate accurate and physically consistent models, even with limited training data.

Index Terms—Dynamic modeling, electric drives, gradient networks, Hamiltonian, magnetic saturation, neural networks, physics-informed machine learning, synchronous machines.

I. INTRODUCTION

DYNAMIC models of electric machines are essential for control, estimation, monitoring, and for the design and optimization of drives. The most challenging aspect of machine modeling is the magnetic model, which describes the relationship between flux linkages, currents, rotor angle, and electromagnetic torque, assuming magnetostatic conditions [1], [2]. In modern power-dense electric machines, magnetic saturation effects are significant and must be incorporated into the models. High-fidelity models that include spatial harmonics are also needed, e.g., in time-domain simulations during the design and optimization stage.

The nonlinear magnetics are modeled using analytical functions [3]–[7], lookup tables [8]–[13], or neural networks [14]–[17]. These models can be characterized based on finite-element method (FEM) data [18], laboratory measurements

This work has been submitted to the IEEE for possible publication. Copyright may be transferred without notice, after which this version may no longer be accessible.

This work was supported in part by the ABB Oy, in part by the Aalto University House of AI, and in part by the Research Council of Finland Centre of Excellence in High-Speed Electromechanical Energy Conversion Systems. The authors acknowledge the use of EPE infrastructure of Aalto School of Electrical Engineering.

Junyi Li, Tim Foßner, Floran Martin, and Marko Hinkkanen are with the Department of Electrical Engineering and Automation, Aalto University, 02150 Espoo, Finland (e-mail: junyi.li@aalto.fi; tim.foissner@aalto.fi; floran.martin@aalto.fi; marko.hinkkanen@aalto.fi).

Antti Piippo is with ABB Oy, Drives, 00380 Helsinki, Finland (e-mail: antti.piippo@fi.abb.com).

[19], or automatic identification routines [20]. The accuracy of the analytical models is limited, and they are difficult to extend to higher dimensions (e.g., for spatial harmonics or multi-phase machines). Lookup tables work well in two dimensions but suffer from the curse of dimensionality, high memory requirements, and non-smooth output when using linear interpolation. Black-box neural networks can approximate high-dimensional complex maps and require less memory than lookup tables, but their training still demands large datasets, their extrapolation capability is limited, and energy balance is not guaranteed.

To address the limitations of black-box neural networks, physics-informed neural networks combine data with known physical principles [21]–[24]. Hamiltonian neural networks [23], [24] are particularly relevant in this context, as electric machines are port-Hamiltonian systems [25] with magnetic field energy serving as the Hamiltonian. According to fundamental physical principles [1], [2], the current vector and electromagnetic torque are the gradients of the field energy with respect to the flux-linkage vector and rotor angle, respectively.

The Hamiltonian neural network architectures [23], [24] model the Hamiltonian as a neural network and obtain the gradients via numerical differentiation. This approach improves data efficiency and physical consistency compared to black-box networks. However, it still faces challenges related to numerical differentiation of the scalar neural network to obtain gradients [26].

Recent gradient networks [26] directly model conservative vector fields, enabling universal approximation of any gradient field without the need for numerical differentiation of a scalar neural network. This approach allows the model to inherently satisfy physical laws such as energy balance and reciprocity, while also improving data efficiency and generalization.

In this paper, we propose a physics-informed magnetic modeling framework for synchronous machines that combines fundamental electromechanical dynamics [1], [2] with gradient networks [26]. The stator current and electromagnetic torque are directly modeled as gradients of a scalar field energy function, which guarantees physical consistency by design. We employ monotone gradient networks to ensure the field energy is convex. This property enforces a unique, invertible relationship between flux linkages and currents, enabling the formulation of both current and flux-linkage (dual) maps. Additionally, Fourier features [27] are incorporated to capture spatial harmonics while preserving the lossless (conservative) field structure. The resulting model offers a universal approximation of complex magnetic behavior, including cross-

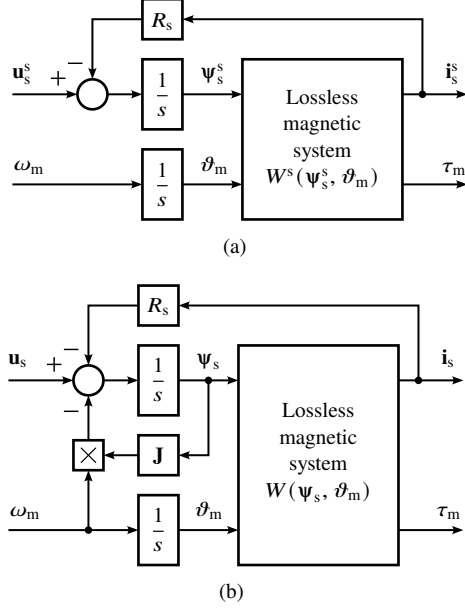


Fig. 1. Electromechanical dynamics of a generic synchronous machine: (a) stator coordinates; (b) rotor coordinates. The blocks $1/s$ denote integration in time.

saturation and angle dependency. We also compare activation functions and propose a computationally efficient p -norm gradient activation as an alternative to the commonly used softmax.

This paper is organized as follows. Section II reviews the physics-based machine model. Section III details the proposed gradient network architecture. In Section IV, the model is validated using measured and FEM datasets from a 5.6-kW permanent-magnet (PM) synchronous reluctance machine. Results demonstrate accurate and physically consistent models, even with limited training data. Section V concludes the paper.

II. PHYSICS-BASED MACHINE MODEL

Scalars are denoted by italic letters (e.g., x), column vectors by bold lowercase letters (e.g., \mathbf{x}), and matrices by bold uppercase letters (e.g., \mathbf{A}). All quantities are in per-unit unless otherwise specified.

A. Stator Coordinates

Fig. 1(a) shows the block diagram of a generic synchronous machine model in stator ($\alpha\beta$) coordinates. The corresponding state equations are

$$\frac{d\psi_s^s}{dt} = \mathbf{u}_s^s - R_s \mathbf{i}_s^s \quad (1a)$$

$$\frac{d\theta_m}{dt} = \omega_m \quad (1b)$$

where $\psi_s^s = [\psi_\alpha, \psi_\beta]^\top$ is the stator flux-linkage vector, $\mathbf{i}_s^s = [i_\alpha, i_\beta]^\top$ is the stator current vector, $\mathbf{u}_s^s = [u_\alpha, u_\beta]^\top$ is the stator voltage vector, and R_s is the stator resistance. Furthermore, θ_m is the electrical angle of the rotor d-axis with respect to the stator coordinates, and ω_m is the electrical angular speed of the rotor.

Assuming a lossless (conservative) magnetic field system, the magnetic behavior is fully described by its field energy function

$W^s(\psi_s^s, \theta_m)$. Hence, the stator current and electromagnetic torque are given by [1], [2]

$$\mathbf{i}_s^s = \left[\frac{\partial W^s(\psi_s^s, \theta_m)}{\partial \psi_s^s} \right]^\top \quad (2a)$$

$$\tau_m = -\frac{\partial W^s(\psi_s^s, \theta_m)}{\partial \theta_m} \quad (2b)$$

where per-unit values are used. The minus sign appears in the torque expression since the positive mechanical power is defined out of the machine. It can be realized that the current and the electromagnetic torque (with negative sign) constitute the gradient of the field energy function.

B. Rotor Coordinates

The machine model is more convenient to express in rotor (dq) coordinates, which rotates with the rotor d-axis. Coordinate transformation to rotor coordinates can be expressed using the matrix exponential as

$$\psi_s = e^{-\theta_m \mathbf{J}} \psi_s^s \quad (3)$$

where $\mathbf{J} = \begin{bmatrix} 0 & -1 \\ 1 & 0 \end{bmatrix}$ is the orthogonal rotation matrix. The flux-linkage vector $\psi_s = [\psi_d, \psi_q]^\top$ is used as an example, but other vectors can be transformed similarly.

1) *Model Structure*: Using (3), the state equations (1) can be transformed to rotor coordinates as

$$\frac{d\psi_s}{dt} = \mathbf{u}_s - R_s \mathbf{i}_s - \omega_m \mathbf{J} \psi_s \quad (4a)$$

$$\frac{d\theta_m}{dt} = \omega_m \quad (4b)$$

where $\mathbf{i}_s = [i_d, i_q]^\top$ is the current vector and $\mathbf{u}_s = [u_d, u_q]^\top$ is the voltage vector. Fig. 1(b) shows the corresponding block diagram.

The field energy function can be expressed in rotor coordinates, $W(\psi_s, \theta_m) = W^s(\psi_s^s, \theta_m)$. Applying the coordinate transformation and the chain rule (see Appendix A), the magnetic model (2) becomes

$$\mathbf{i}_s = \left[\frac{\partial W(\psi_s, \theta_m)}{\partial \psi_s} \right]^\top \quad (5a)$$

$$\tau_m = \mathbf{i}_s^\top \mathbf{J} \psi_s - \frac{\partial W(\psi_s, \theta_m)}{\partial \theta_m} \quad (5b)$$

For a conservative magnetic system, the current map $\mathbf{i}_s(\psi_s, \theta_m)$ is monotone in ψ_s [1]. Mathematically, this means that the incremental inverse inductance matrix $\mathbf{\Gamma}_s = \partial \mathbf{i}_s / \partial \psi_s$ is positive definite, corresponding to a strictly convex energy function $W(\psi_s, \theta_m)$ with respect to ψ_s . In contrast, the dependence on θ_m is generally non-monotone and periodic due to rotational symmetry.

2) *q-Axis Symmetry Without Spatial Harmonics*: If spatial harmonics are omitted and the d-axis is aligned with the PM flux, the field energy is even with respect to the q-axis flux linkage, i.e.,

$$W(\psi_s) = W(\mathbf{C} \psi_s) \quad \mathbf{C} = \text{diag}(1, -1) \quad (6)$$

where the matrix \mathbf{C} conjugates the q-axis flux linkage. To enforce this symmetry, we define the symmetrized energy function

$$\bar{W}(\psi_s) = \frac{1}{2} [W(\psi_s) + W(\mathbf{C} \psi_s)] \quad (7)$$

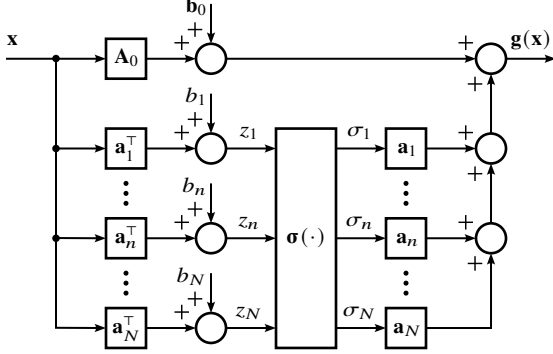


Fig. 2. Gradient network used for the magnetic models.

for which the condition (6) holds by construction. The symmetrized energy preserves both the conservative structure and convexity, since reflecting and averaging convex functions yields a convex function.

Omitting spatial harmonics and using the symmetrized energy (7), the magnetic model (5) simplifies to¹

$$\mathbf{i}_s = \left[\frac{\partial \bar{W}(\Psi_s)}{\partial \Psi_s} \right]^\top \quad (8a)$$

$$\tau_m = \mathbf{i}_s^\top \mathbf{J} \Psi_s \quad (8b)$$

This model guarantees the reflectional symmetry expected in the absence of spatial harmonics. The current map satisfies $i_d(\psi_d, -\psi_q) = i_d(\psi_d, \psi_q)$ and $i_q(\psi_d, -\psi_q) = -i_q(\psi_d, \psi_q)$. Consequently, $i_q(\psi_d, 0) = 0$ holds for all ψ_d .

When spatial harmonics are included, the field energy depends on the rotor angle and the current and torque become periodic in ϑ_m . The strict q-axis symmetry need not hold in that case.

3) *Co-Energy-Based Dual Model*: Alternatively, the dual model $\Psi_s(\mathbf{i}_s, \vartheta_m)$ can be formulated. The field energy W and co-energy W' are related through the Legendre transform $W(\Psi_s, \vartheta_m) + W'(\mathbf{i}_s, \vartheta_m) = \mathbf{i}_s^\top \Psi_s$. This relationship yields the dual model

$$\Psi_s = \left[\frac{\partial W'(\mathbf{i}_s, \vartheta_m)}{\partial \mathbf{i}_s} \right]^\top \quad (9a)$$

$$\tau_m = \mathbf{i}_s^\top \mathbf{J} \Psi_s + \frac{\partial W'(\mathbf{i}_s, \vartheta_m)}{\partial \vartheta_m} \quad (9b)$$

Note that the sign of the partial derivative term in the torque expression is positive.

The choice between the energy-based model (5) and the co-energy-based dual model (9) depends on the application, i.e., whether the current map $\mathbf{i}_s(\Psi_s, \vartheta_m)$ or the flux-linkage map $\Psi_s(\mathbf{i}_s, \vartheta_m)$ is preferred. Due to strict convexity, these maps are invertible.

¹Naturally, this model includes the magnetically linear case, where the field energy is $\bar{W}(\Psi_s) = (\Psi_s - \Psi_f)^\top \Gamma_s (\Psi_s - \Psi_f)/2$, with the constant inverse inductance matrix $\Gamma_s = \text{diag}(1/L_d, 1/L_q)$ and the PM-flux vector $\Psi_f = [\psi_f, 0]^\top$. In this case, the model reduces to the conventional linear relationship $\mathbf{i}_s = \Gamma_s(\Psi_s - \Psi_f)$.

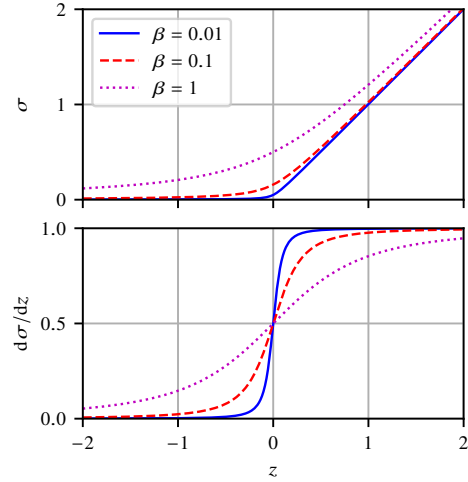


Fig. 3. Elementwise squareplus activation σ in (11) and its derivative $d\sigma/dz$ at different values of parameter β . The shape of the algebraic sigmoid (12) is the same as the derivative of the squareplus, but shifted vertically and scaled.

III. PROPOSED MAGNETIC MODELS BASED ON GRADIENT NETWORKS

A. Gradient Networks

1) *Structure*: Gradient networks can universally approximate any monotone conservative field [26]. We use an architecture with N hidden units, illustrated in Fig. 2. It can be expressed as

$$\mathbf{z} = \mathbf{Ax} + \mathbf{b} \quad (10a)$$

$$\mathbf{g}(\mathbf{x}) = \mathbf{A}_0 \mathbf{x} + \mathbf{b}_0 + \mathbf{A}^\top \sigma(\mathbf{z}) \quad (10b)$$

where $\mathbf{z} = [z_1 \dots z_N]^\top$ is the pre-activation vector, $\mathbf{A}^\top = [\mathbf{a}_1 \dots \mathbf{a}_N]$ is the transposed weight matrix, $\mathbf{b} = [b_1 \dots b_N]^\top$ is the bias vector, and $\sigma(\mathbf{z})$ is the activation vector. The linear output term is defined by the bias vector \mathbf{b}_0 and the symmetric positive semidefinite matrix \mathbf{A}_0 . The activation vector is selected such that its Jacobian $\mathbf{J}_\sigma = \partial \sigma / \partial \mathbf{z}$ is symmetric and positive semidefinite. If elementwise activations $\sigma(\mathbf{z}) = [\sigma_1(z_1) \dots \sigma_N(z_N)]^\top$ are used, they are non-decreasing.

The network (10) is inherently conservative, i.e., it has symmetric Jacobian $\mathbf{J}_g = \partial g / \partial x$, see Appendix B. Furthermore, it is monotone since the Jacobian \mathbf{J}_g is positive semidefinite. Consequently, there exists a convex state function $W(\mathbf{x})$ such that $\mathbf{g}(\mathbf{x}) = [\partial W(\mathbf{x}) / \partial \mathbf{x}]^\top$. However, the state function $W(\mathbf{x})$ does not need to be explicitly modeled, which is a key advantage of the gradient network architecture.

2) *Elementwise Activations*: The activation function $\sigma(\mathbf{z})$ can be chosen in various ways. The simplest choice is elementwise activations, where each component of the output depends only on the corresponding component of the input. Typically, they are computationally more efficient than vector activations. However, elementwise activations cannot universally approximate all monotone conservative fields. They represent only a subset of such fields, corresponding to gradients of sums of convex ridge functions [26].

Elementwise activations must be selected to match the saturation characteristics of the target map. Hence, different

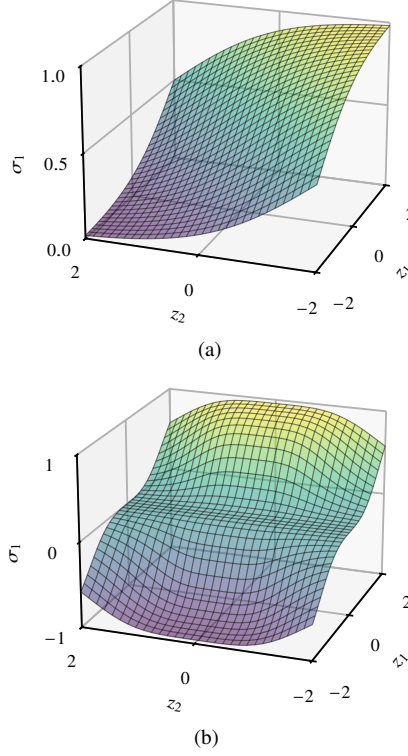


Fig. 4. Vector activation $\sigma_1(z_1, z_2)$ visualized in two-dimensional case: (a) softmax (13) with $\beta = 1$; (b) p -norm gradient (14) with $p = 4$ and $\beta = 1$.

activation types are used for the current and flux-linkage maps. For simplicity, we employ the same activation function for all hidden units within each network.

For modeling current maps, rectifier-type activations, such as softplus or algebraic squareplus, can be used. The squareplus is given by [28]

$$\sigma(z) = \frac{1}{2} \left(z + \sqrt{z^2 + \beta} \right) \quad (11)$$

where the positive parameter β affects the shape around zero. Fig. 3 shows the shape of squareplus $\sigma(z)$ and its derivative $d\sigma/dz = (1 + z/\sqrt{z^2 + \beta})/2$ at different values of β . The derivative smoothly transitions from zero to one, resembling the saturation characteristics of magnetic materials. The squareplus function is computationally more efficient than softplus. It is also inherently numerically stable for large inputs.

For modeling flux-linkage maps, sigmoid-type activations (such as tanh) are more suitable. We use the algebraic sigmoid activation

$$\sigma(z) = \frac{z}{\sqrt{z^2 + \beta}} \quad (12)$$

where the positive parameter β affects the slope around zero. The shape of (12) is the same as the derivative of the squareplus shown in Fig. 3, but shifted vertically and scaled.

3) *Vector Activations*: Vector activations output a vector whose components depend on all elements of the input, unlike elementwise activations, which apply a scalar function

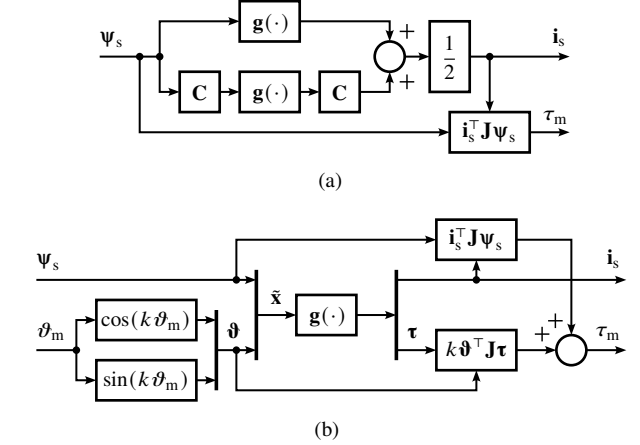


Fig. 5. Proposed magnetic models in rotor coordinates: (a) without spatial harmonics, q-axis symmetry by construction; (b) with spatial harmonics. In both cases, the function $g(\cdot)$ is given by (10).

independently to each input component. The scaled softmax activation is a common choice for vector activations, given by

$$\sigma(\mathbf{z}) = \frac{1}{\sum_{n=1}^N e^{\beta z_n}} \begin{bmatrix} e^{\beta z_1} \\ \vdots \\ e^{\beta z_N} \end{bmatrix} \quad (13)$$

where the positive learnable parameter β affects the shape of the activation. Fig. 4(a) shows the shape of the first component $\sigma_1(z_1, z_2)$ in the two-dimensional case. The softmax is the gradient of the log-sum-exp function $S(\mathbf{z}) = \log(\sum_{n=1}^N e^{\beta z_n})/\beta$. As shown in [26], the gradient network (10) with the softmax activation can universally approximate any monotone conservative field.

As a computationally more efficient alternative to the softmax function, a p -norm gradient can be used, given by

$$\sigma(\mathbf{z}) = \frac{1}{[1 + \sum_{n=1}^N (\beta z_n)^p]^{\frac{p-1}{p}}} \begin{bmatrix} (\beta z_1)^{p-1} \\ \vdots \\ (\beta z_N)^{p-1} \end{bmatrix} \quad (14)$$

where p is a positive even integer and β is a positive learnable parameter. This activation is the gradient of the smooth p -norm $S(\mathbf{z}) = [1 + \sum_{n=1}^N (\beta z_n)^p]^{(1/p)}/\beta$, which is convex, thus guaranteeing monotonicity. The integer powers can be calculated using simple multiplication, which is fast. The only expensive operation is the fractional power, but it is needed only once per forward pass, regardless of the number N of hidden units. In our context, the integer p can typically be 6 or 8, corresponding to the exponent values used in similar low-dimensional models for iron saturation [3], [4], [20].

Unlike elementwise activations, the vector activations (13) and (14) can be used with both current and flux-linkage maps. The p -norm gradient offers computational efficiency and, in our experiments, provided comparable accuracy and robustness to the softmax.

B. Incorporating Physical Symmetries

1) *Without Spatial Harmonics*: When spatial harmonics are omitted, the field energy depends only on the flux linkages. If

TABLE I
RATED VALUES OF THE 5.6-kW PM SYNCHRONOUS
RELUCTANCE MACHINE

Voltage (line-to-neutral, peak value)	$\sqrt{2/3} \cdot 460$ V	1.00 p.u.
Current (peak value)	$\sqrt{2} \cdot 8.8$ A	1.00 p.u.
Frequency	60 Hz	1.00 p.u.
Speed	1 800 r/min	1.00 p.u.
Power	5.6 kW	0.80 p.u.
Torque	29.7 Nm	0.80 p.u.

the symmetry condition (6) is not enforced, we may directly parametrize the current map $\mathbf{i}_s = \mathbf{g}(\psi_s)$ using the monotone gradient network (10). As discussed in Section II-B, the current map is monotone, corresponding to convexity of the field energy $W(\psi_s)$. We use $\mathbf{A}_0 = \text{diag}(\mu_d, \mu_q)$ to encode strong convexity on the d- and q-axes. This architecture guarantees that the learned current $\mathbf{i}_s(\psi_s)$ is the gradient of a μ -strongly convex function, ensuring a unique current for each flux linkage and enabling robust model inversion.

The symmetry condition (6) can be enforced using the symmetrized energy function (7). Differentiating (7) with respect to ψ_s gives the current map

$$\mathbf{i}_s(\psi_s) = \frac{1}{2} [\mathbf{g}(\psi_s) + \mathbf{C} \mathbf{g}(\mathbf{C}\psi_s)] \quad (15)$$

This map $\mathbf{i}_s(\psi_s)$ remains a monotone gradient network, and its Jacobian is positive semidefinite. Fig. 5(a) shows the block diagram for this magnetic model. By construction, the model satisfies q-axis symmetry.

2) *With Spatial Harmonics:* Spatial harmonics introduce angle dependence in the magnetic model (5), making both the current $\mathbf{i}_s(\psi_s, \vartheta_m)$ and the torque term $\partial W / \partial \vartheta_m$ periodic in the rotor angle ϑ_m . To avoid discontinuities at the angle boundaries, we use Fourier features [27]

$$\vartheta = \begin{bmatrix} \cos(k\vartheta_m) \\ \sin(k\vartheta_m) \end{bmatrix} \quad (16a)$$

where k determines the electrical symmetry (e.g., $k = 6$ for a 60° electrical period). The field energy can then be expressed as $W(\psi_s, \vartheta_m) = \tilde{W}(\psi_s, \vartheta)$. With this change of variables and the chain rule, the model (5) becomes

$$\mathbf{i}_s = \left[\frac{\partial \tilde{W}(\psi_s, \vartheta)}{\partial \psi_s} \right]^\top \quad (16b)$$

$$\tau_m = \mathbf{i}_s^\top \mathbf{J} \psi_s + k \vartheta^\top \mathbf{J} \left[\frac{\partial \tilde{W}(\psi_s, \vartheta)}{\partial \vartheta} \right]^\top \quad (16c)$$

Fig. 5(b) shows the block diagram for this magnetic model, where $\tilde{\mathbf{x}} = [\psi_s^\top, \vartheta^\top]^\top$ is the combined input to the monotone gradient network and $\tau = [\partial \tilde{W}(\psi_s, \vartheta) / \partial \vartheta]^\top$ is the gradient with respect to the Fourier features. In the monotone gradient network (10), we use $\mathbf{A}_0 = \text{diag}(\mu_d, \mu_q, 0, 0)$. This adds a linear term proportional to the flux linkages to the output, which enforces μ -strong monotonicity with respect to the flux linkages while leaving the angle features unaffected. By construction, there exists a scalar function $\tilde{W}(\tilde{\mathbf{x}})$ such that $\mathbf{g}(\tilde{\mathbf{x}}) = [\partial \tilde{W}(\tilde{\mathbf{x}}) / \partial \tilde{\mathbf{x}}]^\top$, thus the gradient network preserves the conservative structure of the magnetic model.



Fig. 6. Test bench including a 5.6-kW PM synchronous reluctance machine (left), load machine (right), and their inverter cabinet (background).

By representing the rotor angle through periodic features (16a), the field energy $\tilde{W}(\psi_s, \vartheta)$ is modeled by a monotone gradient network. As a result, the current map $\mathbf{i}_s(\psi_s, \vartheta_m)$ is strictly monotone in ψ_s for each ϑ_m , and both the current and torque are periodic in ϑ_m by construction. This approach enforces the monotonicity and periodicity required by the physical system.

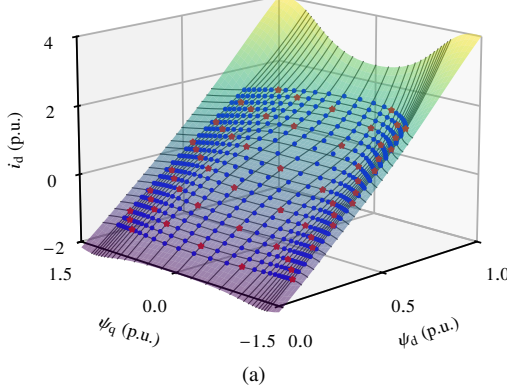
IV. RESULTS

Measured and FEM datasets from a four-pole 5.6-kW PM synchronous reluctance machine were used to validate the proposed magnetic models. Table I lists the rated values of the machine, and Fig. 6 shows the test bench used for measurements. Due to the rotor flux barriers, a small effective air gap in the q-axis direction, and the presence of PMs, the machine has highly nonlinear magnetic characteristics. The results are presented in per-unit values with base values derived from the rated values in Table I. Training was implemented in Python using the *PyTorch* library and AdamW optimizer.

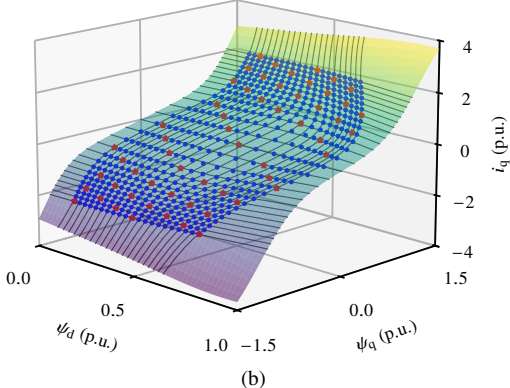
A. Measured Dataset Without Spatial Harmonics

1) *Dataset:* The flux linkages of the example machine were measured on an equidistant current grid using the constant-speed test [19]. By exploiting q-axis symmetry in the measurement procedure, the dataset contains 21×13 unique measurement points. Both d- and q-axis flux linkages were measured at each point. Figs. 7 and 8 show this dataset in flux-linkage coordinates and current coordinates, respectively. For illustration, both positive and negative q-axis values are shown, yielding a full grid of 21×27 points in each map (567 displayed values per map).²

²The measured dataset is available in an example of the *motulator* open-source project: https://aalto-electric-drives.github.io/motulator/drive_examples/flux_vector/plot_6kw_pmsyrm_sat_fvc.html.

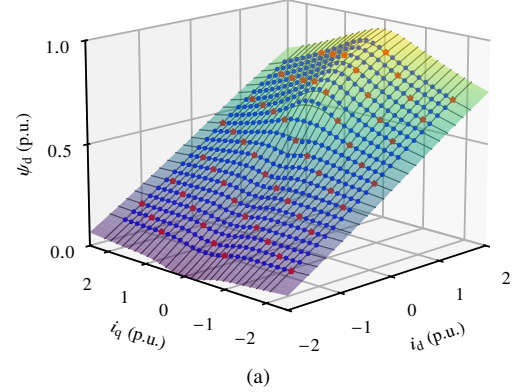


(a)

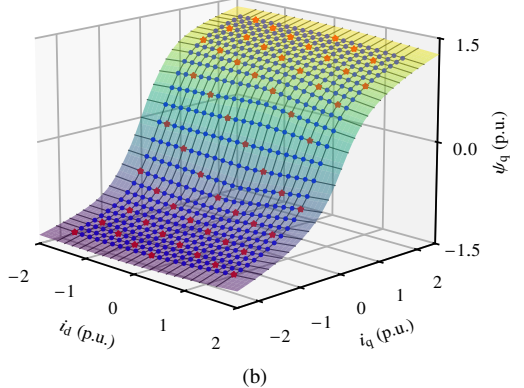


(b)

Fig. 7. Current maps: (a) $i_d(\psi_d, \psi_q)$; (b) $i_q(\psi_d, \psi_q)$. The surfaces show the predicted maps from the p -norm gradient model (14) with $p = 8$ and $N = 12$ hidden units, trained on a 10% subset. Markers show the measured dataset: red indicates the 10% training subset and blue the remaining points. Gray lines show constant-current contours corresponding to the measured dataset.



(a)



(b)

Fig. 8. Flux-linkage maps: (a) $\psi_d(i_d, i_q)$; (b) $\psi_q(i_d, i_q)$. The surfaces show the predicted maps from the p -norm gradient model (14) with $p = 8$ and $N = 12$ hidden units, trained on a 10% subset. Markers show the same measured dataset as in Fig. 7: red indicates the 10% training subset and blue the remaining points. Gray lines show constant-current contours corresponding to the measured dataset.

TABLE II
COMPARISON OF ACTIVATION FUNCTIONS IN CURRENT MAPS WITHOUT SPATIAL HARMONICS ($N = 12$)

Activation	Training data	e_{rms} (p.u.)	e_{max} (p.u.)	e_{std} (p.u.)
squareplus (11)	10%	0.017	0.070	0.011
	2%	0.076	0.344	0.054
softmax (13)	10%	0.031	0.226	0.021
	2%	0.108	0.407	0.068
p -norm gradient (14)	10%	0.021	0.110	0.012
	2%	0.096	0.389	0.061

2) *Model Configuration:* Both energy-based current maps $\mathbf{i}_s(\psi_s)$ and co-energy-based flux-linkage maps $\psi_s(\mathbf{i}_s)$ were trained using the proposed approach. The q-axis symmetry is enforced by construction, see Fig. 5(a). Different activation functions (11)–(14) are compared.

The magnetic models without spatial harmonics have two scalar inputs and two scalar outputs. The number of learnable parameters depends on the number N of hidden units. The models have an $N \times 2$ weight matrix \mathbf{A} , an $N \times 1$ bias vector \mathbf{b} , a 2×2 diagonal output matrix \mathbf{A}_0 , a 2×1 output bias \mathbf{b}_0 , and a single learnable activation parameter β . Consequently, the total number of learnable parameters is $3N + 5$. In the following, we use $N = 12$, resulting in 41 learnable parameters. This number of parameters is small compared to the lookup-table approach.

TABLE III
COMPARISON OF ACTIVATION FUNCTIONS IN FLUX-LINKAGE MAPS WITHOUT SPATIAL HARMONICS ($N = 12$)

Activation	Training data	e_{rms} (p.u.)	e_{max} (p.u.)	e_{std} (p.u.)
algebraic	10%	0.016	0.044	0.010
	2%	0.051	0.165	0.032
softmax (13)	10%	0.007	0.033	0.004
	2%	0.029	0.081	0.019
p -norm gradient (14)	10%	0.004	0.022	0.003
	2%	0.018	0.061	0.012

The mean squared error (MSE) loss was used for training current maps, defined as

$$\mathcal{L} = \frac{1}{L} \sum_{\ell=1}^L \|\mathbf{i}_{s\ell} - \hat{\mathbf{i}}_{s\ell}(\psi_{s\ell})\|^2 \quad (17)$$

where L is the number of training samples, $\mathbf{i}_{s\ell}$ is the measured current for sample ℓ , and $\hat{\mathbf{i}}_{s\ell}(\psi_{s\ell})$ is the model prediction for the corresponding flux-linkage input $\psi_{s\ell}$. For training flux-linkage maps, the same procedure was used, replacing the current error with the flux-linkage error.

3) *Model Performance:* Fig. 7 visualizes the learned current maps with the p -norm gradient activation (14), when every tenth data point (10% of the full measured dataset) is used for training and the rest for validation. It can be observed that the model very

accurately captures the measured data. Fig. 8 shows flux-linkage maps learned by training the co-energy-based dual model with the same activation and training dataset. The other activation functions yield visually similar results when trained with 10% of the dataset.

For quantitative comparison, the root-mean-square (rms) error and the standard deviation over the entire measured dataset are computed, respectively, as

$$e_{\text{rms}} = \sqrt{\frac{1}{L} \sum_{\ell=1}^L e_{\ell}^2} \quad e_{\text{std}} = \sqrt{\frac{1}{L} \sum_{\ell=1}^L (e_{\ell} - \bar{e})^2} \quad (18)$$

where $e_{\ell} = \|\mathbf{i}_{s\ell} - \hat{\mathbf{i}}_{s\ell}\|$ and $\bar{e} = \frac{1}{L} \sum_{\ell=1}^L e_{\ell}$. Furthermore, the maximum error $e_{\text{max}} = \max_{\ell} e_{\ell}$ is considered. The above metrics are defined for current maps, but they can be similarly defined for flux-linkage maps by replacing $\mathbf{i}_{s\ell}$ and $\hat{\mathbf{i}}_{s\ell}$ with the corresponding flux linkages.

Table II summarizes the results for current maps when different activation functions are used. The table shows the results for two different training dataset sizes, 10% and 2% of the full measured dataset. In the latter case, every 50th data point is used for training, resulting in only 12 training samples per map. The results show that all models achieve excellent accuracy when trained with 10% of the dataset and good results even with 2% of the dataset. These results indicate that the underlying energy function can be well approximated with a sum of ridge functions.

Table III gives the results for flux-linkage maps. The models with vector activations show better accuracy than those with elementwise activations, especially when the training dataset is limited to 2%. These results suggest that the underlying co-energy function may not be well approximated by a sum of ridge functions, thus requiring vector activations for accurate modeling with limited data.

B. FEM Dataset With Spatial Harmonics

1) *Dataset*: To demonstrate the capability of the proposed model in Fig. 5(b) in capturing spatial harmonics, the same machine was analyzed using FEM under magnetostatic conditions on an equidistant grid in current and rotor angle. For this machine, the flux linkages and the torque are periodic in the electrical angle ϑ_m with a 60° period. The FEM dataset was generated on an equidistant current grid (61×61), ranging from -2.41 to 2.41 p.u., and at 30 equidistant rotor angles from 0° to 60° . The total dataset size is $61 \times 61 \times 30 = 111\,630$ samples. At each operating point, the d- and q-axis flux linkages and the electromagnetic torque were computed.

2) *Model Configuration*: Both the energy-based and co-energy-based models were trained using the proposed approach. For brevity, the results are shown only for the co-energy-based model, but the energy-based model shows similar performance. The vector activations softmax (13) and the p -norm gradient (14) are compared. The training dataset size is either 10% or 0.2% of the full FEM dataset, corresponding to 11 163 and 223 samples, respectively.

The magnetic models with spatial harmonics have four scalar inputs and four scalar outputs. In the following examples, we use

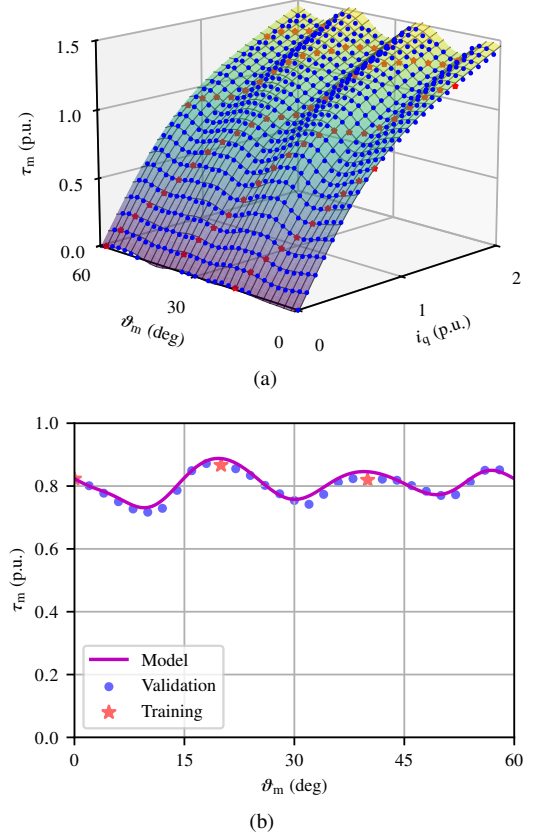


Fig. 9. Electromagnetic torque from the softmax model with $N = 48$ hidden units: (a) $\tau_m(i_d, \vartheta_m)$ at constant i_d corresponding to the rated MTPA current; (b) $\tau_m(\vartheta_m)$ at the constant rated MTPA stator current. The curve and markers in (b) are a slice from (a). Red and blue markers show the full measured dataset. Red markers indicate the 10% training subset.

$N = 48$ hidden units. Therefore, the total number of learnable parameters is $5N + 7 = 247$. The MSE loss is used for training, but it includes both the flux-linkage and torque errors. In the case of the co-energy-based models, the loss function is defined as

$$\mathcal{L} = \frac{1}{L} \sum_{\ell=1}^L \left[\frac{\|\Psi_{s\ell} - \hat{\Psi}_{s\ell}\|^2}{\psi_{\text{max}}^2} + \frac{(\tau_{m\ell} - \hat{\tau}_{m\ell})^2}{\tau_{\text{max}}^2} \right] \quad (19)$$

where ψ_{max} and τ_{max} are the maximum flux linkage and torque in the training dataset, respectively. When training energy-based models, the loss function is defined similarly, replacing the flux linkage error term with the current error term.

3) *Model Performance*: Fig. 9(a) visualizes the proposed co-energy-based model with the softmax activation (13), trained with 10% of the FEM dataset. The model captures both the rotor-angle dependence and the q-axis current dependence of the torque. Fig. 9(b) shows a slice at $i_d = -0.72$ p.u. and $i_q = 0.72$ p.u., which approximately corresponds to the rated maximum-torque-per-ampere (MTPA) current. The torque ripple caused by spatial harmonics is well captured.

Table IV summarizes the prediction errors for flux linkage and torque over the entire FEM dataset. The model achieves good accuracy even when the training dataset is limited to 0.2% of the full FEM dataset. The p -norm gradient activation (14) gives results comparable to the softmax activation (13) when

TABLE IV
COMPARISON OF ACTIVATION FUNCTIONS WITH SPATIAL HARMONICS ($N = 48$)

Activation	Training data	Flux linkage error (p.u.)			Torque error (p.u.)		
		e_{rms}	e_{max}	e_{std}	e_{rms}	e_{max}	e_{std}
softmax (13)	10%	0.008	0.035	0.005	0.012	0.077	0.008
	0.2%	0.011	0.052	0.007	0.016	0.100	0.011
p -norm gradient (14)	10%	0.011	0.042	0.006	0.017	0.086	0.010
	0.2%	0.013	0.081	0.008	0.023	0.214	0.016

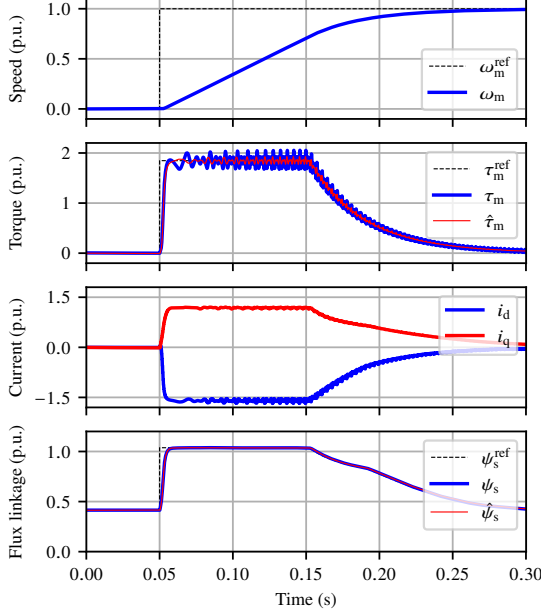


Fig. 10. Simulation example showing acceleration from standstill to 1 p.u. The machine model uses the dynamics (4) and the energy-based model (16) with spatial harmonics. Flux-vector control is applied, parametrized using the co-energy-based dual of (15).

trained with 10% of the dataset, but yields slightly higher errors when trained with 0.2% of the dataset.

4) *Application Examples*: The proposed models can be used for various applications, such as control design and digital twins. Fig. 10 shows a simulation example where the proposed energy-based magnetic model (16) with spatial harmonics is used. This formulation is convenient in simulations, since the flux linkages are states in the dynamics (4), resulting in a straightforward implementation.

In the simulation, a flux-vector control system [29], [30] uses the proposed co-energy-based dual model (i.e., the flux-linkage maps) without spatial harmonics. The flux-linkage maps are convenient in control applications, since the measured stator current is available while the flux linkages must be estimated. The optimal control loci are also computed from these flux-linkage maps. Fig. 11 shows the MTPA trajectory, the maximum-torque-per-voltage (MTPV) trajectory, and three current limits. Owing to the smoothness of the model, these loci are smooth and free from numerical noise, unlike in the case of linear interpolation models.

The machine is accelerated from standstill to 1 p.u. speed, while the maximum current is set to 2 p.u. The effect of spatial

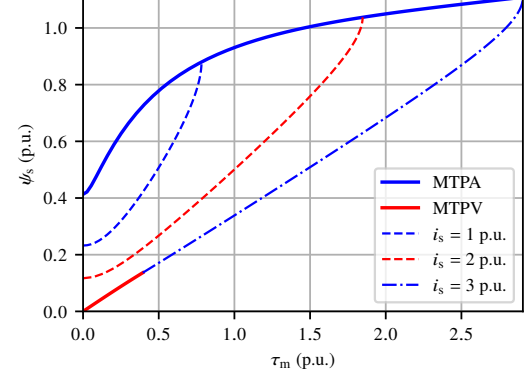


Fig. 11. Optimal control loci computed from the proposed model without spatial harmonics, including the MTPA trajectory, the maximum-torque-per-voltage (MTPV) trajectory, and three current limits.

harmonics is most apparent in the actual torque, but it is also visible in other signals. The proposed models allow physically consistent high-fidelity simulations and provide a universal representation of the machine for control design.

V. CONCLUSIONS

We presented a physics-informed magnetic modeling framework for synchronous machines based on gradient networks. The stator current and the electromagnetic torque are obtained as gradients of a single scalar field energy. This guarantees a conservative field with a symmetric Jacobian (reciprocity) by construction, while the rotor angle input enables periodic dependence and spatial harmonics without breaking the gradient structure. Monotone gradient networks are used to enforce single-valued mapping between the current and flux linkage, corresponding to physical properties of convex field energy and enabling robust inversion. If desired, q-axis symmetry can also be enforced.

These physical properties are embedded in the architecture, improving data efficiency and providing smooth, physically consistent predictions suitable for control and optimization applications, in addition to digital twins. Experiments on measured and FEM data demonstrate that the proposed models are accurate and data-efficient. The presented modeling approach can be extended to other electric machine types.

APPENDIX A TRANSFORMATION TO ROTOR COORDINATES

The same field energy can be expressed in different coordinates, $W(\psi_s, \vartheta_m) = W^s(\psi_s^s, \vartheta_m)$. Using the chain rule with

$\Psi_s^s = e^{\vartheta_m \mathbf{J}} \Psi_s$ gives

$$\frac{\partial W(\Psi_s, \vartheta_m)}{\partial \Psi_s} = \frac{\partial W^s(\Psi_s^s, \vartheta_m)}{\partial \Psi_s^s} \frac{\partial \Psi_s^s}{\partial \Psi_s} = (\mathbf{i}_s^s)^\top e^{\vartheta_m \mathbf{J}} = \mathbf{i}_s^\top \quad (20a)$$

$$\begin{aligned} \frac{\partial W(\Psi_s, \vartheta_m)}{\partial \vartheta_m} &= \frac{\partial W^s(\Psi_s^s, \vartheta_m)}{\partial \Psi_s^s} \frac{\partial \Psi_s^s}{\partial \vartheta_m} + \frac{\partial W^s(\Psi_s^s, \vartheta_m)}{\partial \vartheta_m} \\ &= (\mathbf{i}_s^s)^\top \mathbf{J} \Psi_s^s + \frac{\partial W^s(\Psi_s^s, \vartheta_m)}{\partial \vartheta_m} \end{aligned} \quad (20b)$$

Using $\tau_m = -\partial W^s / \partial \vartheta_m$ yields the expressions in (5).

APPENDIX B JACOBIAN OF THE GRADIENT NETWORK MODEL

The vector field (10) is conservative if its Jacobian \mathbf{J}_g is symmetric [26]. Applying the chain rule, the Jacobian of the gradient network (10) becomes

$$\mathbf{J}_g(\mathbf{x}) = \frac{\partial \mathbf{g}(\mathbf{x})}{\partial \mathbf{x}} = \mathbf{A}_0 + \mathbf{A}^\top \frac{\partial \boldsymbol{\sigma}(\mathbf{z})}{\partial \mathbf{z}} \mathbf{A} \quad (21)$$

The first term \mathbf{A}_0 is chosen to be symmetric. The second term is symmetric if $\mathbf{J}_{\boldsymbol{\sigma}} = \partial \boldsymbol{\sigma} / \partial \mathbf{z}$ is symmetric, which is the case when the activation $\boldsymbol{\sigma}$ is a gradient of a scalar function. Notice that $\mathbf{J}_{\boldsymbol{\sigma}}$ is diagonal and thus symmetric when the activation is elementwise. The network (10) is monotone if \mathbf{J}_g is positive semidefinite. This is guaranteed if \mathbf{A}_0 and $\mathbf{J}_{\boldsymbol{\sigma}}$ are positive semidefinite.

ACKNOWLEDGMENTS

The authors thank Dr. Francesco Lelli, Ari Haavisto, and Hannu Hartikainen for their contributions regarding the measurements on the example machine, located at the EPE infrastructure of Aalto School of Electrical Engineering.

REFERENCES

- [1] H. H. Woodson and J. R. Melcher, *Electromechanical Dynamics*. John Wiley & Sons, 1968. [Online]. Available: https://ocw.mit.edu/ans7870/resources/woodson/textbook/emd_part1.pdf
- [2] A. E. Fitzgerald, C. Kingsley, Jr., and S. D. Umans, *Electric Machinery*, 6th ed. Boston, MA: McGraw-Hill, 2003.
- [3] J. Fischer and U. Moser, "Die Nachbildung von Magnetisierungskurven durch einfache algebraische oder transzendentale Funktionen," *Arch. für Electrotechnik*, vol. 42, no. 5, pp. 286–299, 1956.
- [4] Z. Qu, T. Tuovinen, and M. Hinkkanen, "Inclusion of magnetic saturation in dynamic models of synchronous reluctance motors," in *Proc. Int. Conf. Electrical Machines*, Marseille, France, Sep. 2012, pp. 994–1000.
- [5] M. Gärtner, F. Schuller, N. Parspour, and P. Seibold, "Analytical modeling and simulation of highly utilized electrical machines considering nonlinear effects," in *Proc. Int. Conf. Elect. Machines*, Marseille, France, 2012, pp. 2786–2791.
- [6] A. Varatharajan, P. Pescetto, S. Ferrari, and G. Pellegrino, "Flux maps spatial harmonic modeling and measurement in synchronous reluctance motors," in *Proc. IEEE ECCE*, Nashville, TN, Oct./Nov. 2023, pp. 4868–4873.
- [7] F. Lelli, M. Hinkkanen, and F. G. Capponi, "A saturation model based on a simplified equivalent magnetic circuit for permanent magnet machines," in *Proc. Int. Conf. Elect. Machines*, Torino, Italy, Sep. 2024.
- [8] A. Vagati, M. Pastorelli, G. Franceschini, and V. Drogoreanu, "Flux-observer-based high-performance control of synchronous reluctance motors by including cross saturation," *IEEE Trans. Ind. Appl.*, vol. 35, no. 3, pp. 597–605, May/Jun. 1999.
- [9] X. Chen, J. Wang, B. Sen, P. Lazari, and T. Sun, "A high-fidelity and computationally efficient model for interior permanent-magnet machines considering the magnetic saturation, spatial harmonics, and iron loss effect," *IEEE Trans. Ind. Electron.*, vol. 62, no. 7, pp. 4044–4055, 2015.
- [10] S. Li, D. Han, and B. Sarlioglu, "Modeling of interior permanent magnet machine considering saturation, cross coupling, spatial harmonics, and temperature effects," *IEEE Trans. Transport. Electricific.*, vol. 3, no. 3, pp. 682–693, 2017.
- [11] J. Lee, Y.-C. Kwon, and S.-K. Sul, "Identification of IPMSM flux-linkage map for high-accuracy simulation of IPMSM drives," *IEEE Trans. Power Electron.*, vol. 36, no. 12, pp. 14 257–14 266, 2021.
- [12] S. Ferrari, G. Dilevrano, P. Ragazzo, and G. Pellegrino, "The dq-theta flux map model of synchronous machines," in *Proc. IEEE ECCE*, Vancouver, Canada, Oct. 2021, pp. 3716–3723.
- [13] A. Bojoi, P. Pescetto, S. Ferrari, and G. Pellegrino, "Experimental identification of the dqθ flux maps of synchronous machines," in *Proc. Int. Conf. Elect. Machines*, Turin, Italy, Sep. 2024.
- [14] D. Pasqualotto, S. Rigan, and M. Zigliotto, "Sensorless speed control of synchronous reluctance motor drives based on extended kalman filter and neural magnetic model," *IEEE Trans. Ind. Electron.*, vol. 70, no. 2, pp. 1321–1330, Feb. 2023.
- [15] H. Mohajerani, U. Deshpande, and N. C. Kar, "RNN-based high fidelity permanent magnet synchronous motor emulator considering driving inverter switching faults," *IEEE J. Emerg. Sel. Topics Ind. Electron.*, vol. 5, no. 4, pp. 1420–1434, Oct. 2024.
- [16] ———, "A neural-network-based electric machine emulator using neuro-fuzzy controller for power-hardware-in-the-loop testing," *IEEE Trans. Energy Convers.*, vol. 40, no. 3, pp. 2242–2255, Sep. 2025.
- [17] J.-H. Lee, Y.-J. Lee, M.-S. Lee, D.-S. Jin, and Y.-D. Yoon, "Estimation of flux saturation model for SynRMs using artificial neural network," *IEEE Trans. Ind. Appl.*, vol. 61, no. 2, pp. 3143–3151, 2025.
- [18] M. Carbonieri, L. D. Leonardo, A. Mahmoudi, M. Tursini, N. Bianchi, and W. L. Soong, "Fast flux mapping technique for synchronous reluctance machines: Method description and comparison with full FEA and measurements," *IEEE Trans. Ind. Appl.*, vol. 59, no. 4, pp. 4056–4065, Jul./Aug. 2023.
- [19] E. Armando, R. Bojoi, P. Guglielmi, G. Pellegrino, and M. Pastorelli, "Experimental identification of the magnetic model of synchronous machines," *IEEE Trans. Ind. Appl.*, vol. 49, no. 5, pp. 2116–2125, Sep. 2013.
- [20] M. Hinkkanen, P. Pescetto, E. Mölsä, S. E. Saarakkala, G. Pellegrino, and R. Bojoi, "Sensorless self-commissioning of synchronous reluctance motors at standstill without rotor locking," *IEEE Trans. Ind. Appl.*, vol. 53, no. 3, pp. 2120–2129, May/Jun. 2017.
- [21] M. Raissi, P. Perdikaris, and G. E. Karniadakis, "Physics-informed neural networks: A deep learning framework for solving forward and inverse problems involving nonlinear partial differential equations," *Journal of Computational Physics*, vol. 378, pp. 686–707, 2019.
- [22] M. Cranmer, S. Greydanus, S. Hoyer, P. Battaglia, D. Spergel, and S. Ho, "Lagrangian neural networks," in *ICLR Workshop on Integration of Deep Neural Models and Differential Equations*, 2020. [Online]. Available: <https://arxiv.org/abs/2003.04630>
- [23] S. Greydanus, M. Dzamba, and J. Yosinski, "Hamiltonian neural networks," in *Adv. Neur. Inf. Process. Syst.*, vol. 32, Vancouver, Canada, 2019. [Online]. Available: <https://arxiv.org/abs/1906.01563>
- [24] S. A. Desai, M. Mattheakis, D. Sondak, P. Protopapas, and S. J. Roberts, "Port-Hamiltonian neural networks for learning explicit time-dependent dynamical systems," *Phys. Rev. E*, vol. 104, p. 034312, Sep. 2021.
- [25] A. van der Schaft and D. Jeltsema, *Port-Hamiltonian Systems Theory: An Introductory Overview*. Delft, Netherlands: now Publishers Inc., 2014.
- [26] S. Chaudhari, S. Pranav, and J. M. F. Moura, "Gradient networks," *IEEE Trans. Signal Process.*, vol. 73, pp. 324–339, 2025.
- [27] M. Tancik, P. Srinivasan, B. Mildenhall, S. Fridovich-Keil, N. Raghavan, U. Singh, R. Ramamoorthi, J. Barron, and R. Ng, "Fourier features let networks learn high frequency functions in low dimensional domains," in *Adv. Neur. Inf. Process. Syst.*, vol. 33, 2020. [Online]. Available: <https://arxiv.org/abs/2006.10739>
- [28] J. T. Barron, "Squareplus: A softplus-like algebraic rectifier," 2021. [Online]. Available: <https://arxiv.org/abs/2112.11687>
- [29] L. Tiitinen, M. Hinkkanen, and L. Harnefors, "Design framework for sensorless control of synchronous machine drives," *IEEE Trans. Ind. Electron.*, vol. 72, no. 2, pp. 1379–1390, Feb. 2025.
- [30] A. Varatharajan, G. Pellegrino, and E. Armando, "Direct flux vector control of synchronous motor drives: Accurate decoupled control with online adaptive maximum torque per ampere and maximum torque per volts evaluation," *IEEE Trans. Ind. Electron.*, vol. 69, no. 2, pp. 1235–1243, Feb. 2022.



Junyi Li received the B.Sc. degree in communication engineering from the Taiyuan University of Technology, Taiyuan, China, in 2022, and the M.Sc. (Tech.) degree in information and communication engineering from the Aalto University, Espoo, Finland, in 2025.

He is currently working toward the doctoral degree in automation and electrical engineering at Aalto University. His research interests include condition monitoring and physics-informed machine learning.



Antti Pippoo received the M.Sc. (Eng.) and D.Sc. (Tech.) degrees in electrical engineering from the Helsinki University of Technology, Espoo, Finland, in 2003 and 2008, respectively.

He is currently an R&D Executive Engineer with ABB Oy, Drives, Helsinki, Finland. His main research interests include the control of electric drives.



Tim Foßner received the B.Sc. degrees in electrical engineering and information technology and in mechatronics from TU Darmstadt, Darmstadt, Germany, in 2023 and 2024, respectively.

Since 2024, he has been pursuing the M.Sc. degree in automation and electrical engineering with a specialization in electrical power engineering at Aalto University, Espoo, Finland.



Marko Hinkkanen (M'06–SM'13–F'23) received the M.Sc. (Eng.) and D.Sc. (Tech.) degrees in electrical engineering from the Helsinki University of Technology, Espoo, Finland, in 2000 and 2004, respectively.

He is currently a Full Professor with the School of Electrical Engineering, Aalto University, Espoo, Finland. His research interests include control systems, physics-informed machine learning, electric machine drives, and power converters.

Dr. Hinkkanen was the recipient of eight paper awards, including the 2016 International Conference on Electrical Machines (ICEM) Brian J. Chalmers Best Paper Award, and the 2016 and 2018 IEEE Industry Applications Society Industrial Drives Committee Best Paper Awards. He was the corecipient of the 2020 SEMIKRON Innovation Award. He was the General Cochair of the 2018 IEEE 9th International Symposium on Sensorless Control for Electrical Drives (SLED). He is an Associate Editor of IEEE TRANSACTIONS ON POWER ELECTRONICS.



Floran Martin received the Engineering Diploma in electrical engineering from Polytech Nantes, Nantes, France, in 2009, and the M.S. and Ph.D. degrees in electrical engineering from the University of Nantes, Nantes, in 2009 and 2013, respectively.

In 2014, he joined the Department of Electrical Engineering and Automation, Aalto University, Espoo, Finland, where he is currently a Staff Scientist. His research interests include modeling of magnetic materials as well as analyzing, designing, and controlling electrical machines.